

## Dipole strength in $^{89}\text{Y}$ up to the neutron-separation energy

N. Benouaret,<sup>1,2</sup> R. Schwengner,<sup>2</sup> G. Rusev,<sup>2,\*</sup> F. Dönau,<sup>2</sup> R. Beyer,<sup>2</sup> M. Erhard,<sup>2</sup> E. Grosse,<sup>2,3</sup> A. R. Junghans,<sup>2</sup> K. Kosev,<sup>2</sup> C. Nair,<sup>2</sup> K. D. Schilling,<sup>2</sup> A. Wagner,<sup>2</sup> and N. Bendjabbalah<sup>1</sup>

<sup>1</sup>*Faculté de physique, Université des Sciences et de la Technologie d'Alger, El-Alia 16111, Bab-Ezzouar-Alger, Algeria*

<sup>2</sup>*Institut für Strahlenphysik, Forschungszentrum Dresden-Rossendorf, D-01314 Dresden, Germany*

<sup>3</sup>*Institut für Kern- und Teilchenphysik, Technische Universität Dresden, D-01062 Dresden, Germany*

(Received 23 September 2008; revised manuscript received 18 November 2008; published 12 January 2009)

Photoexcitation of the  $N = 50$  nucleus  $^{89}\text{Y}$  has been performed at the bremsstrahlung facility at the superconducting electron accelerator ELBE at electron energies of  $E_e^{\text{kin}} = 9.5$  and 13.2 MeV. About 250 levels up to the neutron-separation energy were identified. Statistical methods were applied to estimate intensities of inelastic transitions and to correct the intensities of the ground-state transitions for their branching ratios. The photoabsorption cross section derived in this way up to the neutron-separation energy is combined with the photoabsorption cross section obtained from  $(\gamma, n)$  data and provides information about the extension of the giant dipole resonance toward energies below the neutron-separation energy. An enhancement of  $E1$  strength has been found in the range from about 6 to 11 MeV. The experimental photoabsorption cross sections of  $^{89}\text{Y}$  and of the neighboring  $N = 50$  isotones  $^{88}\text{Sr}$  and  $^{90}\text{Zr}$  are compared with predictions of the quasiparticle-random-phase approximation.

DOI: [10.1103/PhysRevC.79.014303](https://doi.org/10.1103/PhysRevC.79.014303)

PACS number(s): 25.20.Dc, 21.10.Tg, 23.20.-g, 27.50.+e

### I. INTRODUCTION

In atomic nuclei, an electric dipole moment is induced by an out-of-phase oscillation of the protons against the neutrons at excitation energies above the neutron-separation energy  $S_n$ . This mode, referred to as the giant dipole resonance (GDR) in the energy range of about 10–20 MeV, is microscopically related to a coherent superposition of  $1p1h$  excitations.

In recent years, high-resolution photon-scattering experiments on even-mass nuclei with a closed  $N = 82$  neutron shell revealed a concentration of intense electric dipole transitions close to the neutron-separation energy [1,2] that cannot be associated with the low-energy tail of the GDR if it is assumed to drop smoothly below the threshold. This excitation mode is called the pygmy dipole resonance (PDR) because the corresponding reduced electric dipole ( $E1$ ) transition strengths are smaller ( $\approx 10^{-3}$  W.u.) than the ones in the GDR ( $\approx 10$  W.u.). Such an excitation mode had already been predicted in a hydrodynamical model [3]. The associated total  $E1$  strengths may indicate a correlation to the excess of the neutron number relative to the proton number. Together with theoretical models using microscopic or macroscopic approaches such as the two-fluid hydrodynamical model [4], the density functional theory [5], and the Hartree Fock plus random phase approximation with Skyrme forces [6,7], pygmy dipole resonances were described as an out-of-phase oscillation of a neutron skin against the  $N \approx Z$  core. Such a behavior has also been experimentally observed in very neutron rich light nuclei [8,9]. Therefore, it is interesting to understand whether the mechanism is the same for nuclei with small or moderate neutron excess.

Moreover, dipole excitations close to the particle threshold are a source of information on the high level density. The corresponding  $\gamma$ -ray strength functions are important input parameters for astrophysical models describing the nucleosynthesis in stars [10] as well as for a better description of  $(n, \gamma)$  reactions used for next-generation nuclear technologies.

Up to now,  $E1$  strength distributions have been investigated in photon-scattering experiments in the  $Z = 20$  isotopes  $^{40,44,48}\text{Ca}$  [11,12], in the  $Z = 50$  isotopes  $^{116,124}\text{Sn}$  [13], in the  $N = 82$  isotones  $^{138}\text{Ba}$ ,  $^{140}\text{Ce}$ , and  $^{144}\text{Sm}$  [2], and in  $^{208}\text{Pb}$  [14]. The nature and systematic features such as the dependence of the centroid energy, the width, and the dependence of the strength of the PDR on  $N/Z$  in each chain remain under discussion. Consequently, new data will shed light on this type of excitation.

We initiated a study of the dipole strength in  $N = 50$  nuclei up to the neutron-separation energy at the bremsstrahlung facility of the ELBE accelerator of the research center Dresden-Rossendorf [15] and studied the nuclides  $^{88}\text{Sr}$  [16] and  $^{90}\text{Zr}$  [17]. The present work investigates the nuclide  $^{89}\text{Y}$  with the odd proton number  $Z = 39$  between the subshell closures at  $Z = 38$  ( $^{88}\text{Sr}$ ) and  $Z = 40$  ( $^{90}\text{Zr}$ ). It therefore provides an interesting case to study the effect of the unpaired proton on the  $E1$  strength function and thus on possible PDR strength. The odd- $A$  nucleus  $^{89}\text{Y}$  has the following single-proton levels up to about 1.8 MeV excitation energy: the  $\pi p_{1/2}$  ground state, the  $\pi g_{9/2}$  isomer, and  $\pi p_{3/2}^{-1}$  and  $\pi f_{5/2}^{-1}$  states [18,19]. The states lying in the region from 2.2 to 4.2 MeV arise from the coupling of the  $0g_{9/2}$  proton to the lowest  $2^+$  and  $3^-$  collective one-phonon states in the  $Z = 38$  core  $^{88}\text{Sr}$  [20] except for the  $3/2^-$  and  $5/2^-$  levels originating from the coupling of the  $p_{1/2}$  hole ground-state configuration to the first excited  $2^+$  state in the  $Z = 40$  neighbor  $^{90}\text{Zr}$  [21]. In spherical even-even nuclei near the shell closure, two-phonon states may result from the coupling of the quadrupole  $2^+$  vibration to an octupole  $3^-$  excitation

\*Present address: Department of Physics, Duke University, Triangle Universities Nuclear Laboratory, Durham, NC 27708, USA.

[22], forming a quintuplet of states with  $1^- \leq J^\pi \leq 5^-$ . The excitation energies of the states of the quintuplet are expected to lie closely below the sum of the excitation energies of the two considered phonons. The  $1^-$  state of this quintuplet can be populated in photon-scattering experiments and has been observed via an intense  $E1$  ground-state transition [23].

In odd- $A$  nuclei, an enhanced  $E1$  transition resulting from the coupling of the odd particle to states of the  $(2_1^+ \otimes 3_1^-)$  multiplet was also identified [24]. In the case of  $^{89}\text{Y}$ , the coupling of the unpaired  $p_{1/2}$  proton to the  $(2_1^+ \otimes 3_1^-)1^-$  states in  $^{88}\text{Sr}$  forming  $1/2^+$  and  $3/2^+$  states has been investigated by means of photon-scattering experiments at  $E_e^{\text{kin}} = 5.0$  MeV [21] and at  $E_e^{\text{kin}} = 7.0$  MeV [25].

The present experiment aims at the study of the dipole strength up to the neutron-separation energy at  $S_n = 11.5$  MeV. The high level density at high excitation energy manifests in spectra of scattered photons including several hundreds of peaks. In addition, it turns out that a considerable portion of the strength is located in a continuum of unresolved peaks. To obtain the correct strength function we have applied statistical methods. By means of simulations of  $\gamma$ -ray cascades we estimate the distribution of inelastic transitions populating low-lying excited states and the branching ratios for the elastic transitions to the ground state, which are needed to deduce the correct photoabsorption cross section.

## II. EXPERIMENTAL TECHNIQUES

Bremsstrahlung was produced by irradiating niobium foils of  $4 \mu\text{m}$  or  $7 \mu\text{m}$  thickness with electron beams delivered by the superconducting electron accelerator ELBE of the research center Dresden-Rossendorf. Two experiments were performed at electron energies of 9.5 and 13.2 MeV with average currents of 520 and 600  $\mu\text{A}$  and measuring times of 78 and 87 h, respectively. A 10-cm-thick aluminum absorber was placed behind the radiator to attenuate the low-energy part of the bremsstrahlung spectrum. The target consisted of 3303.2 mg of natural yttrium powder formed into a disk of about 20 mm in diameter, enabling a uniform photon flux within the beam spot diameter of 38 mm at the target position. The target was combined with 339.5 mg of  $^{11}\text{B}$  enriched to 99.52%, also formed into a disk of 20 mm in diameter and used for the determination of the photon flux.

Scattered photons were measured with four high-purity germanium (HPGe) detectors of about 100% efficiency relative to a  $3 \times 3$  in. NaI detector. Two HPGe detectors were placed at  $\Theta = 90^\circ$  with respect to the incident photon beam at a distance of 28 cm to the target while the other two were positioned at  $\Theta = 127^\circ$  at a distance of 32 cm to the target, corresponding to opening angles of  $16^\circ$  and  $14^\circ$ , respectively. Each HPGe detector was surrounded by an escape-suppression shield made of bismuth-germanate (BGO) scintillation detectors. Details of the setup are given in Ref. [15]. To reduce the intensity of scattered low-energy photons, the detectors at  $90^\circ$  and  $127^\circ$  had absorbers of 13 mm Pb + 3 mm Cu and of 8 mm Pb + 3 mm Cu, respectively, placed in front. The absolute efficiency of the detectors was

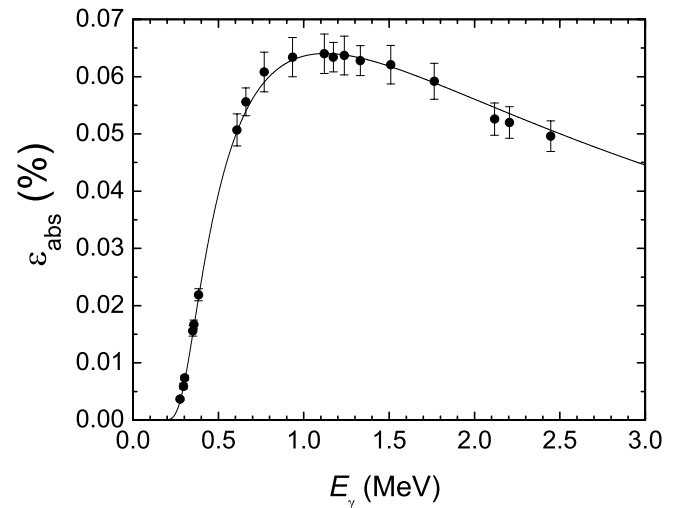


FIG. 1. Absolute efficiency values of the two detectors at  $127^\circ$  determined from standard calibration sources (circles) and efficiency calculated with GEANT3 (solid line).

determined by using  $^{60}\text{Co}$ ,  $^{133}\text{Ba}$ ,  $^{137}\text{Cs}$ , and  $^{226}\text{Ra}$  standard calibration sources. Simulations using the code GEANT3 [26] were performed to extrapolate the efficiency curve to higher energies. Measured and calculated efficiencies are shown in Fig. 1. The reliability of the behavior of the simulated curve was proven by a comparison with relative efficiencies deduced from transitions in  $^{11}\text{B}$  [16]. The absolute photon flux was deduced from the intensities of transitions in  $^{11}\text{B}$  by using the known integrated scattering cross sections. For interpolation the flux was calculated with a code [27] based on the approximation given in Ref. [28] and including a screening correction according to Ref. [29]. The photon flux used for the analysis is shown in Fig. 2.

Integrated scattering cross sections  $I_s$  were calculated relative to the ones known for transitions in  $^{11}\text{B}$  by using

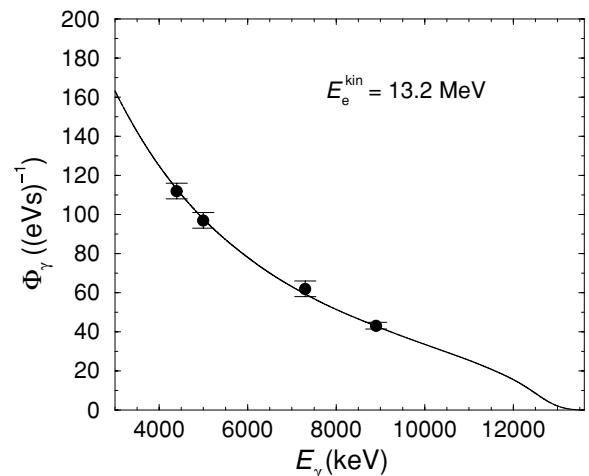


FIG. 2. Absolute photon flux deduced from transitions in  $^{11}\text{B}$  (circles) and calculated photon flux (solid line).

efficiency-corrected intensities of the observed transitions:

$$I_s(E_x) = I_s(E_x^B) \cdot \frac{I_\gamma(E_\gamma, \Theta)}{I_\gamma(E_\gamma^B, \Theta)} \cdot \frac{W(E_\gamma^B, \Theta) N_N^B}{W(E_\gamma, \Theta) N_N} \cdot \frac{\Phi_\gamma(E_x^B)}{\Phi_\gamma(E_x)} \quad (1)$$

Here,  $I_\gamma(E_\gamma, \Theta)$  and  $I_\gamma(E_\gamma^B, \Theta)$  denote the intensities of a considered ground-state transition at  $E_\gamma$  and of a ground-state transition in  $^{11}\text{B}$  at  $E_\gamma^B$ , respectively, detected at an angle  $\Theta$  relative to the beam and  $N_N$  and  $N_N^B$  are the numbers of nuclei in the target and in  $^{11}\text{B}$ , respectively. The ratio  $\Phi_\gamma(E_x^B)/\Phi_\gamma(E_x)$  is the ratio of the photon flux at the energy of a ground-state transition from a level at  $E_x$  in  $^{11}\text{B}$  to the one at the energy of the considered transition. The quantities  $W(E_\gamma, \Theta)$  and  $W(E_\gamma^B, \Theta)$  are the angular correlations of the considered transition and the one in  $^{11}\text{B}$ , respectively. The partial width of the ground-state transition,  $\Gamma_0$ , from an excited level with spin  $J$  to the ground state with spin  $J_0$  relates to the integrated scattering cross section according to

$$I_s = \int \sigma_{\gamma\gamma} dE = \frac{2J+1}{2J_0+1} \left( \frac{\pi\hbar c}{E_x} \right)^2 \frac{\Gamma_0^2}{\Gamma}, \quad (2)$$

where  $\Gamma$  is the total level width.

### III. EXPERIMENTAL RESULTS

Spectra of photons scattered from  $^{89}\text{Y}$  measured at  $127^\circ$  relative to the beam are shown in Figs. 3 and 4 for the electron energies of 9.5 and 13.2 MeV, respectively. To improve the statistics, the spectra of the detectors at  $127^\circ$  to the beam were added.

The comparison of spectra measured at different electron energies can be used to discriminate between elastic ground-state transitions and inelastic transitions to low-lying excited levels. All transitions observed up to 7 MeV in the measurements at electron energies of 9.5 and 13.2 MeV but not found in the measurement at 7 MeV [25] are considered as inelastic transitions from levels at energies greater than 7 MeV. Analogously, transitions up to 9.5 MeV observed only in the measurement at 13.2 MeV are considered as inelastic transitions from levels above 9.5 MeV. A consequence of inelastic transitions is that part of the intensity of the ground-state transition at low energy arises from feeding by higher lying states in addition to the direct excitation from the ground state. Hence, the integrated cross section  $I_{s+f}$  deduced from this intensity contains a part originating from feeding  $I_f$  in addition to the true integrated scattering cross section:  $I_{s+f} = I_s + I_f$ . To estimate the effect of feeding on the ground-state transitions, we deduced ratios of integrated cross sections obtained at different electron energies. The values for  $E_e^{\text{kin}} = 7.0$  MeV were taken from Ref. [25]. Feeding is indicated by a deviation from unity. The ratios are displayed in Fig. 5 and listed in Table I. One sees that levels below about 6 MeV are considerably influenced by feeding, mainly from levels above 9 MeV. The increase of the ratios including the values at  $E_e^{\text{kin}} = 7.0$  MeV taken from Ref. [25] above  $E_x \approx 6.5$  MeV may indicate a systematic uncertainty in this measurement (e.g., an overestimate of the photon flux toward the endpoint of the bremsstrahlung spectrum).

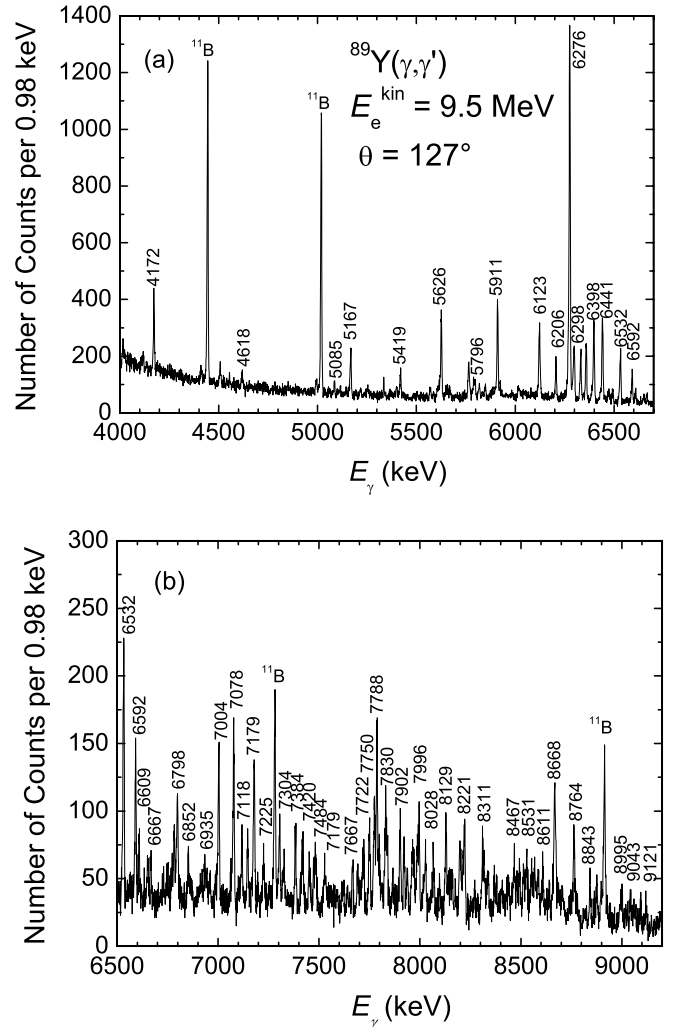


FIG. 3. Parts of a spectrum of photons scattered from  $^{89}\text{Y}$  combined with  $^{11}\text{B}$  at an electron energy of 9.5 MeV. This spectrum contains events of the two detectors at  $127^\circ$ .

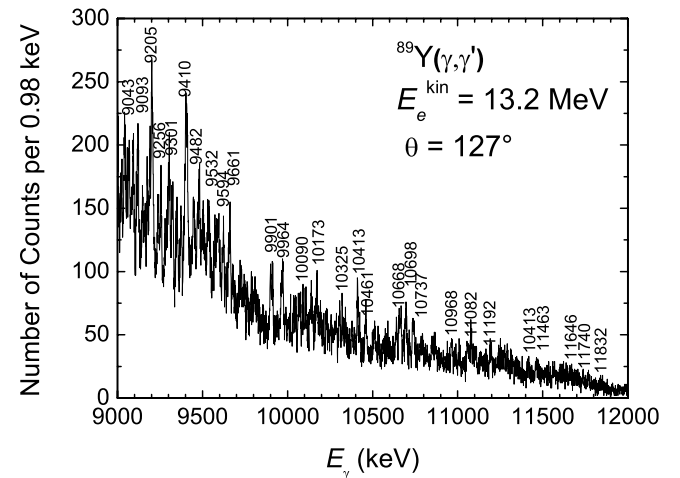


FIG. 4. Part of a spectrum of photons scattered from  $^{89}\text{Y}$  combined with  $^{11}\text{B}$  at an electron energy of 13.2 MeV. This spectrum contains events of the two detectors at  $127^\circ$ .

TABLE I. Levels assigned to  $^{89}\text{Y}$ .

$E_x$ (keV) <sup>a</sup>	$\frac{I_\gamma(90^\circ)}{I_\gamma(127^\circ)}$ <sup>b</sup>	$\frac{I_{s+f}(9.5)}{I_{s+f}(7.0)}$ <sup>c</sup>	$\frac{I_{s+f}(13.2)}{I_{s+f}(7.0)}$ <sup>c</sup>	$\frac{I_{s+f}(13.2)}{I_{s+f}(9.5)}$ <sup>c</sup>	$I_s$ (eV b) <sup>d</sup>	$g\Gamma_0^2/\Gamma$ (meV) <sup>e</sup>
1508.0(2)	0.99(4)				134(14)	79(8)
2881.7(2)	0.91(6)				67(7)	145(15)
3067.7(2)	1.06(9)	3.6(7)	14.7(27)	4.1(6)	43(5)	105(12)
3107.7(2)	1.20(18)	3.6(8)	17.7(31)	4.9(8)	21(3)	53(7)
3139.5(3)	1.22(27)	4.4(10)	23.3(47)	5.1(9)	20(3)	51(8)
3516.6(2)	1.06(16)	7.6(10)	37(30)	4.9(7)	19(2)	61(8)
3992.4(2)	0.81(9)	1.3(2)	3.2(5)	2.6(4)	35(4)	145(16)
4171.7(3)	1.07(13)	1.0(2)	2.2(3)	2.3(4)	23(3)	104(13)
4617.8(15)	1.30(48)	1.8(7)	1.9(6)	1.1(4)	7(2)	39(12)
4625.8(5)	0.97(77)			2.4(2)	2(1)	11(6)
4993.5(15)	0.81(38)	1.5(6)	3.1(10)	2.0(8)	6(2)	39(13)
5085.4(6)	0.92(30)	1.6(5)	4.0(10)	2.6(6)	8(2)	54(13)
5167.7(3)	0.81(8)	0.8(2)	1.1(2)	1.3(2)	30(4)	208(28)
5419.4(5)	0.69(14)	1.1(2)	1.6(3)	1.5(3)	17(3)	130(23)
5614.4(15)	1.00(33)			0.7(3)	6(2)	49(16)
5625.8(2)	0.89(6)	0.9(2)	1.1(2)	1.2(2)	63(7)	519(58)
5653.9(15)	1.07(63)	0.8(4)	2.5(10)	3.2(17)	6(3)	50(25)
5789.4(8)	0.74(19)			1.7(4)	10(2)	87(17)
5796.4(8)	1.20(26)	7.3(2)	1.5(4)	2.0(5)	11(2)	96(17)
5910.7(2)	0.90(6)	0.8(2)	0.9(2)	1.0(1)	74(8)	673(73)
5923.4(9)	0.48(22)	0.6(2)	0.87(2)	1.4(4)	8(2)	73(18)
6122.9(2)	0.81(7)	1.0(2)	1.1(2)	1.2(2)	79(9)	771(50)
6206.3(3)	1.08(14)	1.5(4)	1.0(5)	1.0(2)	35(5)	350(50)
6275.6(2)	0.88(4)	1.0(2)	1.1(2)	1.0(1)	409(43)	4191(441)
6297.6(3)	0.93(10)	1.3(3)	1.4(3)	1.1(2)	70(8)	722(83)
6331.6(3)	0.78(8)	1.1(3)	1.2(3)	1.1(2)	53(6)	552(63)
6359.1(2)	1.03(8)	1.2(3)	1.3(3)	1.0(2)	60(7)	631(74)
6398.2(2)	1.07(7)	1.3(3)	1.5(3)	1.2(2)	95(10)	1012(107)
6441.5(2)	1.04(6)	1.4(3)	1.4(3)	1.0(1)	96(10)	1036(108)
6472.3(18)	1.17(47)	2.1(1)	2.3(10)	1.2(5)	12(4)	131(44)
6479(3)	0.66(34)			0.6(5)	7(3)	76(33)
6493.5(8)	1.28(37)	2.8(11)	2.6(9)	0.9(3)	18(4)	197(44)
6532.3(3)	0.96(7)	1.5(4)	1.7(4)	1.1(2)	69(8)	766(89)
6592.2(3)	0.94(12)	1.8(5)	2.4(6)	1.3(2)	37(5)	418(57)
6608.9(5)	1.13(22)	2.3(8)	3.9(1)	1.7(4)	17(3)	193(34)
6651.6(8)	1.26(35)			2.1(6)	12(3)	138(35)
6666.8(8)	1.12(32)			2.2(6)	12(3)	139(35)
6728(2)	1.17(55)			4.3(18)	5(2)	59(24)
6751.1(12)	1.40(39)			1.4(4)	8(2)	95(24)
6772.0(14)	0.87(26)			1.1(3)	9(2)	107(24)
6782.9(6)	0.86(14)			1.4(3)	21(3)	251(36)
6798.2(5)	0.88(11)			1.2(2)	35(5)	421(60)
6852.4(8)	1.10(31)			1.2(3)	17(3)	208(37)
6866(2)	2.81(152)			2.0(11)	5(2)	61(25)
6921(2)	1.40(67)				4(2)	50(25)
6934.7(11)	0.93(20)			1.1(2)	11(2)	138(25)
6944.5(12)	0.91(23)			1.1(3)	10(2)	125(25)
6959.6(14)	0.41(22)			7.2(3)	8(2)	101(25)
6987.4(15)	0.58(27)			1.1(4)	7(2)	89(25)
7003.8(3)	0.83(7)			9.7(1)	57(6)	728(77)
7066.8(15)	1.14(31)			1.5(4)	10(2)	130(26)
7077.7(3)	1.00(9)			1.1(2)	65(8)	847(104)
7106(3)	1.76(89)			1.3(7)	5(2)	66(26)
7118.2(6)	0.84(14)			1.0(2)	23(3)	303(40)
7147.1(6)	0.76(13)			1.0(2)	25(4)	332(53)
7178.6(3)	0.80(7)			1.1(2)	59(7)	791(94)
7198(2)	1.11(59)			1.3(7)	6(2)	81(27)

TABLE I. (Continued.)

$E_x$ (keV) <sup>a</sup>	$\frac{I_y(90^\circ)}{I_y(127^\circ)}$ <sup>b</sup>	$\frac{I_{s+f}(9.5)}{I_{s+f}(7.0)}$ <sup>c</sup>	$\frac{I_{s+f}(13.2)}{I_{s+f}(7.0)}$ <sup>c</sup>	$\frac{I_{s+f}(13.2)}{I_{s+f}(9.5)}$ <sup>c</sup>	$I_s$ (eV b) <sup>d</sup>	$g\Gamma_0^2/\Gamma$ (meV) <sup>e</sup>
7225.3(8)	1.03(25)			1.0(3)	23(5)	312(68)
7240(3)	1.12(79)			0.3(2)	7(4)	95(55)
7255(3)	0.80(69)				4(2)	55(27)
7304.4(5)	0.89(12)			1.1(2)	32(4)	444(56)
7325.4(9)	1.27(28)			1.1(3)	15(3)	209(42)
7383.7(5)	0.98(12)			1.0(2)	33(4)	468(57)
7420.4(8)	0.90(16)			2.3(5)	29(5)	416(72)
7452.1(8)	0.94(22)			1.1(3)	23(5)	332(72)
7475.2(15)	0.94(24)			0.9(3)	18(4)	262(58)
7484.1(11)	0.90(20)			1.0(2)	25(5)	364(73)
7527.9(14)	0.5422			1.2(3)	20(4)	295(59)
7536(3)	0.54(38)			1.3(1)	10(3)	148(44)
7548(5)	0.23(19)				5(3)	74(44)
7556(4)	1.05(47)			0.7(4)	8(3)	119(45)
7566(3)	0.48(34)				7(3)	104(45)
7588.1(18)	0.44(25)				10(3)	150(45)
7618.4(9)	1.10(28)			1.3(4)	15(3)	227(45)
7640.8(11)	0.97(33)			2.9(8)	12(3)	182(46)
7652.3(20)	0.63(42)			4.2(17)	7(3)	107(46)
7666.1(6)	0.97(22)			1.3(4)	26(5)	398(76)
7692.2(8)	0.70(17)			1.0(2)	22(4)	339(62)
7703.3(15)	1.03(36)			1.6(5)	11(3)	170(46)
7714.0(14)	0.89(25)			0.9(3)	18(4)	279(62)
7722.2(9)	0.75(19)			1.4(3)	27(5)	419(78)
7750.5(5)	0.89(10)			1.1(2)	50(6)	782(94)
7774.4(5)	0.90(8)			1.1(2)	61(7)	959(110)
7787.5(3)	1.03(7)			1.1(2)	101(11)	1594(174)
7799.2(8)	0.83(13)			1.0(2)	30(4)	475(63)
7811.8(17)	1.04(33)			1.1(4)	12(3)	191(48)
7830.2(6)	0.88(11)			1.1(2)	57(7)	909(112)
7838.7(8)	0.68(13)			0.9(2)	36(5)	576(80)
7866.8(17)	0.46(26)			0.8(4)	18(7)	290(112)
7902.5(5)	0.89(15)			1.0(2)	50(8)	812(130)
7920.5(3)	0.43(131)			1.5(6)	15(5)	245(82)
7922.7(2)	1.99(1.1)			1.3(3)	19(2)	310(33)
7937.8(9)	1.10(29)			0.9(3)	24(5)	393(82)
7961.7(11)	0.77(26)			0.8(2)	32(6)	528(99)
7968.8(9)	0.91(33)			0.9(2)	34(6)	562(99)
7986.0(8)	0.63(14)			0.9(2)	41(6)	680(100)
7996.1(5)	1.03(17)			0.9(2)	66(9)	1098(150)
8018(2)	0.92(50)			1.2(5)	11(4)	184(67)
8027.7(8)	0.97(14)			1.0(2)	34(5)	570(84)
8067.3(5)	0.72(9)			1.2(3)	32(6)	542(102)
8099.0(14)	0.47(25)			7.0(2)	16(4)	273(68)
8129.3(3)	0.89(7)			1.1(2)	69(9)	1187(155)
8142.1(12)	1.10(22)			1.2(4)	19(5)	328(86)
8150.8(17)	1.02(27)			0.8(2)	23(5)	398(86)
8159.7(9)	0.98(20)			1.0(2)	28(5)	485(87)
8175.6(9)	0.86(20)			1.0(3)	19(5)	330(87)
8198.9(5)	0.81(8)			0.9(2)	63(8)	1102(140)
8210.9(8)	0.93(14)			1.0(2)	30(6)	526(105)
8221.2(3)	0.91(7)			1.2(2)	73(10)	1284(176)
8270.7(6)	1.27(44)			0.9(3)	19(5)	338(89)
8285.4(17)	2.41(160)			0.7(4)	9(4)	161(71)
8311.0(5)	0.93(12)			1.1(2)	45(7)	809(126)
8320.1(6)	1.02(14)			1.0(2)	40(6)	721(108)
8330.4(14)	0.68(20)			1.5(6)	14(5)	253(90)

TABLE I. (*Continued.*)

$E_x$ (keV) <sup>a</sup>	$\frac{I_\gamma(90^\circ)}{I_\gamma(127^\circ)}$ <sup>b</sup>	$\frac{I_{s+f}(9.5)}{I_{s+f}(7.0)}$ <sup>c</sup>	$\frac{I_{s+f}(13.2)}{I_{s+f}(7.0)}$ <sup>c</sup>	$\frac{I_{s+f}(13.2)}{I_{s+f}(9.5)}$ <sup>c</sup>	$I_s$ (eV b) <sup>d</sup>	$g\Gamma_0^2/\Gamma$ (meV) <sup>e</sup>
8338.1(8)	0.71(12)			1.3(3)	31(6)	561(109)
8369(2)	0.37(21)			2.2(1)	17(4)	310(73)
8380.0(9)	0.67(31)			2.5(1)	16(4)	292(73)
8403.1(9)	1.05(46)			2.4(7)	19(4)	349(73)
8438.0(8)	0.64(14)			1.7(5)	21(5)	389(93)
8455(4)	0.43(43)			0.6(4)	15(4)	279(74)
8466.9(8)	0.84(15)			1.5(3)	42(7)	783(131)
8483.2(9)	0.87(20)			1.1(3)	31(5)	580(94)
8495.2(8)	0.65(15)			1.4(3)	35(6)	657(113)
8513.5(5)	0.67(11)			1.2(3)	39(7)	736(132)
8530.6(8)	0.80(24)			1.1(2)	53(8)	1004(151)
8548.3(12)	0.79(20)			0.9(3)	28(7)	532(133)
8556.0(9)	0.55(15)			1.8(6)	18(6)	343(114)
8568.0(6)	0.67(11)			1.4(3)	36(7)	688(134)
8586.9(6)	0.68(13)			1.2(3)	36(7)	691(134)
8603(3)	1.00(66)				10(5)	193(96)
8610.8(12)	0.77(38)			1.3(5)	33(8)	637(154)
8642.1(8)	0.70(30)				20(6)	389(117)
8668.0(5)	1.00(10)			0.9(2)	168(22)	3284(430)
8764.2(3)	0.91(7)			1.2(2)	97(13)	1939(260)
8779.3(11)	0.98(20)				16(5)	321(100)
8843.4(5)	0.63(11)			1.4(4)	55(12)	1119(244)
8864(4)	1.95(171)				17(7)	348(143)
8877.3(5)	0.96(13)			0.9(2)	55(12)	1128(246)
8899.3(6)	0.72(12)			1.0(3)	41(9)	845(185)
8926.3(14)	0.49(32)				23(5)	477(104)
8981(3)	1.41(60)				13(5)	273(105)
8994.5(17)	0.84(22)				39(8)	821(168)
9002.8(15)	1.26(29)				41(9)	865(190)
9024.2(9)	1.04(26)				30(6)	636(127)
9043.4(6)	0.83(14)				59(8)	1256(170)
9057.8(15)	1.06(26)				29(6)	619(128)
9069.0(11)	0.73(16)				48(7)	1027(150)
9082(2)	0.82(37)				18(5)	386(107)
9093.4(8)	0.79(18)				53(9)	1140(194)
9112.7(19)	0.32(27)				25(6)	540(130)
9121.4(8)	0.75(22)				50(11)	1082(238)
9147.0(9)	0.99(26)				31(6)	675(131)
9161.2(14)	0.78(27)				22(5)	480(109)
9175.7(9)	0.78(20)				31(5)	679(110)
9191.2(8)	0.78(14)				44(6)	967(132)
9204.5(5)	0.79(9)				90(10)	1984(220)
9240.0(6)	0.95(17)				39(6)	859(122)
9256.1(6)	0.90(17)				45(7)	1003(156)
9280.2(15)	0.92(44)				17(4)	381(90)
9290.8(15)	0.76(15)				21(4)	472(90)
9301.1(12)	0.31(5)				48(8)	1081(180)
9308.4(14)	1.46(39)				39(7)	879(158)
9320(2)	0.53(38)				24(8)	542(181)
9326.7(11)	1.21(31)				44(9)	996(204)
9351.2(8)	0.66(19)				55(12)	1251(273)
9374.7(8)	0.40(18)				59(16)	1349(366)
9401.8(18)	1.08(33)				63(16)	1449(368)
9410.0(17)	1.25(26)				77(17)	1774(392)
9449.6(9)	1.64(31)				46(7)	1069(163)
9471(3)	0.17(41)				24(7)	560(163)
9482.0(15)	1.43(39)				55(10)	1287(234)

TABLE I. (Continued.)

$E_x$ (keV) <sup>a</sup>	$\frac{I_y(90^\circ)}{I_y(127^\circ)}$ <sup>b</sup>	$\frac{I_{s+f}(9.5)}{I_{s+f}(7.0)}$ <sup>c</sup>	$\frac{I_{s+f}(13.2)}{I_{s+f}(7.0)}$ <sup>c</sup>	$\frac{I_{s+f}(13.2)}{I_{s+f}(9.5)}$ <sup>c</sup>	$I_s$ (eV b) <sup>d</sup>	$g\Gamma_0^2/\Gamma$ (meV) <sup>e</sup>
9503(3)	0.33(28)				37(15)	869(353)
9532(4)	0.51(43)				31(14)	733(331)
9541(3)	1.99(84)				33(12)	782(284)
9575.6(18)	1.58(66)				42(9)	1002(215)
9593.6(15)	1.43(50)				52(11)	1245(263)
9623.7(11)	0.90(23)				33(7)	795(169)
9660.9(8)	1.01(16)				48(7)	1166(170)
9679.4(2)	1.33(59)				12(5)	293(122)
9901.0(8)	1.04(20)				31(5)	791(128)
9912.0(8)	1.03(22)				30(5)	767(128)
9964.2(9)	0.96(20)				22(4)	568(103)
9973.2(6)	0.62(11)				36(5)	932(129)
9990.3(12)	0.79(28)				12(3)	312(78)
10005.8(15)	0.56(32)				9(3)	234(78)
10017.6(18)	0.68(45)				8(3)	209(78)
10037.4(15)	0.38(20)				22(8)	577(210)
10049(2)	0.50(33)				21(11)	552(289)
10065(4)	0.20(15)				19(14)	501(369)
10073.9(19)	0.64(55)				26(20)	687(528)
10091.3(14)	0.41(31)				25(16)	662(424)
10108.2(14)	0.66(43)				25(15)	665(399)
10141.3(12)	0.68(19)				40(9)	1070(241)
10173.0(11)	0.71(18)				45(8)	1212(215)
10194.5(24) <sup>f</sup>	0.59(36)				20(5)	541(135)
10276.2(19)	0.36(35)				11(5)	302(137)
10286.9(19)	0.96(34)				18(5)	496(138)
10307.1(11)	0.73(20)				28(5)	774(138)
10324.5(12)	0.46(17)				23(4)	638(111)
10340.5(15)	0.24(18)				18(4)	501(111)
10379.3(9)	1.07(41)				14(4)	392(112)
10395.0(12)	0.46(17)				11(3)	309(84)
10412.7(7)	0.74(14)				39(5)	1100(141)
10424.8(9)	0.96(26)				19(3)	537(85)
10460.9(18)	0.67(27)				28(8)	797(228)
10469(6)	1.81(151)				7(5)	200(143)
10504(5)					9(4)	258(115)
10513.8(15)					21(6)	604(173)
10538.1(19)					13(5)	376(144)
10641.6(11)					25(5)	737(147)
10659.7(18)					25(5)	739(148)
10668.2(11)					28(6)	829(178)
10697.4(8)					35(6)	1042(179)
10736.8(14)					29(8)	870(240)
10744.5(18)					25(7)	751(210)
10753(3)					11(5)	331(150)
10967.5(11)					25(6)	782(188)
11058.9(15)					19(4)	605(127)
11069(2)					13(4)	414(128)
11081.8(9)					26(5)	831(160)
11106.9(18)					12(4)	385(128)
11192.5(19)					18(7)	587(228)
11200(2)					14(6)	457(196)
11419.3(14)					19(4)	645(136)
11463.0(18)					18(4)	615(137)
11474(3)					10(4)	343(137)
11498(3)					7(4)	241(138)
11517(2)					8(5)	276(173)

TABLE I. (*Continued.*)

$E_x$ (keV) <sup>a</sup>	$\frac{I_\gamma(90^\circ)}{I_\gamma(127^\circ)}$ <sup>b</sup>	$\frac{I_{s+f}(9.5)}{I_{s+f}(7.0)}$ <sup>c</sup>	$\frac{I_{s+f}(13.2)}{I_{s+f}(7.0)}$ <sup>c</sup>	$\frac{I_{s+f}(13.2)}{I_{s+f}(9.5)}$ <sup>c</sup>	$I_s$ (eV) <sup>d</sup>	$g\Gamma_0^2/\Gamma$ (meV) <sup>e</sup>
11535.9(5)					6(2)	208(69)
11560.7(6)					8(3)	278(104)
11571.2(8)					6(3)	209(105)
11601.8(17)					9(4)	315(140)
11611(2)					7(3)	246(105)
11623(3)					9(4)	316(141)
11646.0(19)					7(4)	247(142)
11660.4(14)					10(7)	354(248)
11669.3(18)					7(6)	248(213)
11691.4(18)					7(5)	249(178)
11739.8(12)					13(3)	466(108)
11770.0(12)					12(3)	433(108)
11802(2)					9(4)	326(145)
11817(3)					5(2)	182(73)
11832.1(15)					10(4)	364(146)
11843(2)					6(3)	219(109)
11854(2)					8(3)	293(110)
11873.5(19)					5(3)	183(110)
11913.2(14)					8(3)	295(111)
11946.9(18)					4(2)	149(74)
11962.3(14)					5(2)	186(74)
11984(2)					3(2)	112(75)
11991(2)					4(2)	150(75)

<sup>a</sup>Excitation energy. The uncertainty in parentheses is given in units of the last digit. This value was deduced from the  $\gamma$ -ray energy measured at  $127^\circ$  by including a recoil and Doppler-shift correction.

<sup>b</sup>Ratio of the intensities measured at angles of  $90^\circ$  and  $127^\circ$ . The expected values for a pure dipole transition and the spin sequence  $1/2-3/2-1/2$  and for a quadrupole transition and the spin sequence  $1/2-5/2-1/2$  are 0.87 and 1.15, respectively.

<sup>c</sup>Ratio of integrated scattering plus feeding cross sections deduced at different electron energies. The deviation from unity is a measure of feeding. The values of  $I_{s+f}$  at  $E_e^{\text{kin}} = 7.0$  MeV were taken from Ref. [25].

<sup>d</sup>Integrated scattering cross section. The values up to the level at 8899 keV were deduced from the measurement at  $E_e^{\text{kin}} = 9.5$  MeV; the values given for levels at higher energies were deduced from the measurement at  $E_e^{\text{kin}} = 13.2$  MeV.

<sup>e</sup>Partial width of the ground-state transition  $\Gamma_0$  multiplied with the branching ratio  $\Gamma_0/\Gamma$  and the statistical factor  $g = (2J + 1)/(2J_0 + 1)$ .

<sup>f</sup>The corresponding ground-state transition may include a small contribution from a transition following the  $^{73}\text{Ge}(n, \gamma)$  reaction in the detectors.

Transitions assumed as ground-state transitions in  $^{89}\text{Y}$  were used to derive the corresponding level energies. These are listed in Table I together with ratios of intensities measured at  $90^\circ$  and  $127^\circ$ , integrated cross sections, and partial widths of the ground-state transitions. The intensity ratios  $I_\gamma(90^\circ)/I_\gamma(127^\circ)$  are expected to have values of 0.87 for a pure dipole transition and the spin sequence  $1/2-3/2-1/2$  and 1.15 for a quadrupole transition and the spin sequence  $1/2-5/2-1/2$ . Because most of the experimental ratios are too uncertain for a definite assignment, no spin values are given for the identified levels. As a consequence, only the quantity  $g\Gamma_0^2/\Gamma$  with  $g = (2J + 1)/(2J_0 + 1)$  can be deduced from the integrated scattering cross section according to Eq. (2). However, we found in the neighboring  $N = 50$  isotones  $^{88}\text{Sr}$  [16] and  $^{90}\text{Zr}$  [17] that all transitions above about 6 MeV are dipole transitions. Therefore, dipole character is also assumed for the transitions in  $^{89}\text{Y}$  above 6 MeV in the following discussion.

The detection limit, defined as twice the statistical uncertainty of the area of a background window with a length corresponding to the full width at half maximum of a peak at the same energy, is shown in terms of reduced partial width times the branching ratio  $\Gamma_0^2/(\Gamma E_\gamma^3)$  in Fig. 6 for the measurement at  $E_e^{\text{kin}} = 13.2$  MeV under the assumption of dipole transitions ( $g = 2$ ).

Although the measurements at different energies helped to identify ground-state transitions, they do not enable a definite and complete assignment of inelastic transitions to particular levels. Moreover, the high level density at high excitation energy causes many weak transitions that are not resolved as peaks but form a continuum part in the spectrum (see Sec. IV). To estimate the intensity distribution of the inelastic transitions and to deduce the correct dipole-strength distribution from the full intensity distribution including resolved peaks as well as the continuum part, we have applied statistical methods described in the following.

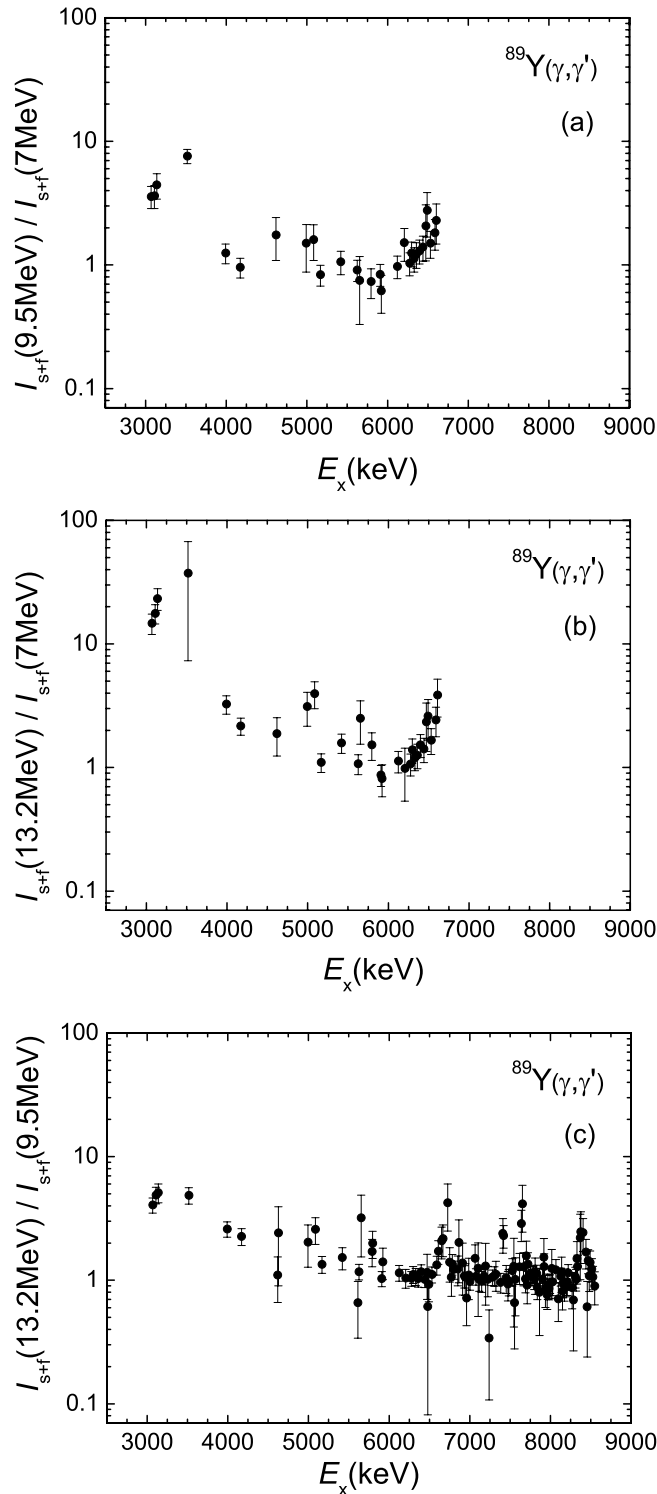


FIG. 5. Ratios of integrated cross section  $I_{s+f}$  obtained at different electron energies.

#### IV. DETERMINATION OF THE DIPOLE-STRENGTH DISTRIBUTION

To prepare the experimental spectrum for the statistical analysis we subtracted spectra of the ambient background adjusted to the intensities of the 1460.5-keV transition (decay

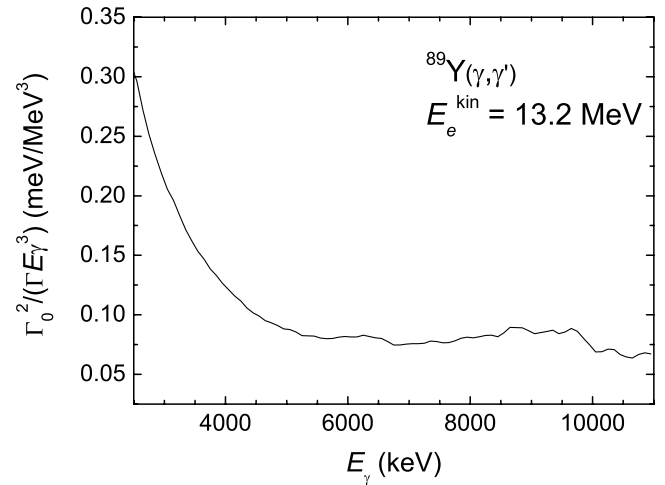


FIG. 6. Detection limit in units of the reduced partial width times the branching ratio in the measurement at 13.2 MeV.

of  $^{40}\text{K}$ ) and 2614.9-keV transition (decay of  $^{208}\text{Tl}$ ) in the in-beam spectrum. Although the maximum energy of the bremsstrahlung (13.2 MeV) exceeds the threshold for the  $(\gamma, n)$  reaction (11.5 MeV) and neutrons may be produced that hit the detectors, it turned out that transitions following  $(n, \gamma)$  reactions in the HPGe detectors and in surrounding materials are negligibly small and did not require correction. To correct the spectrum for detector response, spectra of monoenergetic  $\gamma$  rays were calculated in steps of 10 keV by using GEANT3 [16,17,30]. Starting from the high-energy end of the experimental spectrum, the simulated spectra were subtracted sequentially. The resulting spectrum including the two detectors at  $127^\circ$  is shown in Fig. 7.

The background produced by atomic processes in the  $^{89}\text{Y}$  target was also obtained from a GEANT3 simulation by using the absolute photon flux deduced from the intensities of the transitions in  $^{11}\text{B}$ . The corresponding background spectrum

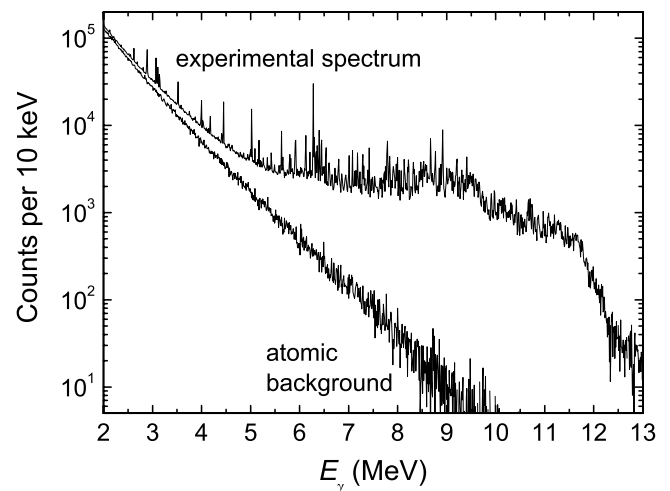


FIG. 7. Experimental spectrum of  $^{89}\text{Y}$  measured at  $E_e^{\text{kin}} = 13.2$  MeV and  $\Theta = 127^\circ$ , corrected for room background and detector response, and simulated spectrum of atomic background, multiplied with efficiency and measuring time.

multiplied with the efficiency curve and with the measuring time is also shown in Fig. 7. The continuum in the spectrum of photons scattered from  $^{89}\text{Y}$  is clearly higher than the background by atomic scattering above about 4 MeV. This continuum is formed by a large number of nonresolvable transitions with small intensities; these are a consequence of the increasing nuclear level density at high energy and of Porter-Thomas fluctuations of the decay widths [31] in connection with the finite detector resolution (e.g.,  $\Delta E \approx 7$  keV at  $E_\gamma \approx 9$  MeV).

The relevant intensity of the photons resonantly scattered from  $^{89}\text{Y}$  is obtained from a subtraction of the atomic background from the response-corrected experimental spectrum. The remaining intensity distribution includes the intensity contained in the resolved peaks as well as the intensity of the “nuclear” continuum. The scattering cross sections  $\sigma_{\gamma\gamma'}$  derived from this intensity distribution for energy bins of 0.2 MeV are shown in Fig. 8. These values are compared with those given in Table I for resolved transitions in  $^{89}\text{Y}$ . The two curves have similar structures caused by the prominent peaks. However, the curve including also the continuum part of the spectrum contains altogether a strength that is by a factor of about 4 greater than the strength of the resolved peaks only.

The full intensity distribution (resolved peaks and continuum) shown in Fig. 8 contains ground-state transitions and, in addition, branching transitions to lower lying excited states (inelastic transitions) as well as transitions from those states to the ground state (cascade transitions). For the determination of the photoabsorption cross section and the

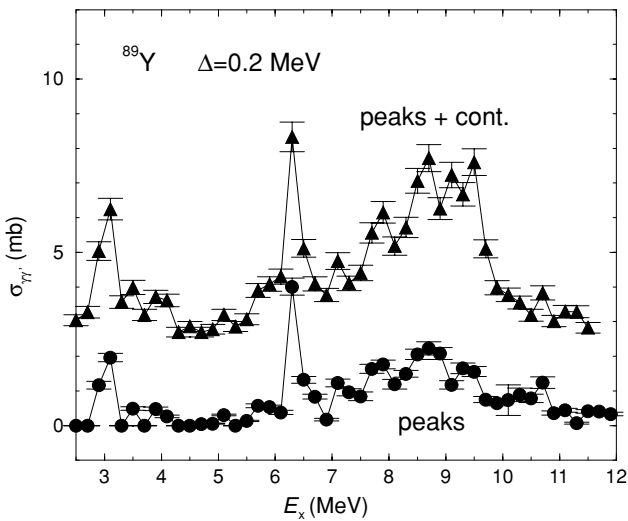


FIG. 8. Scattering cross sections in  $^{89}\text{Y}$ , derived as  $\sigma_{\gamma\gamma'} = \sum_{\Delta} I_s / \Delta$ , not corrected for branching and averaged over energy bins of  $\Delta = 0.2$  MeV, derived from the full intensity distribution obtained from subtraction of the atomic background from the experimental spectrum at  $E_e^{\text{kin}} = 13.2$  MeV shown in Fig. 7 (triangles) and derived from the resolved peaks given in Table I only (circles). Note that the cross sections of the peaks around 3 MeV included in “peaks + cont” are influenced by feeding whereas the cross sections of the resolved peaks were deduced from the measurement at 7.0 MeV and do not include considerable feeding intensities.

partial widths  $\Gamma_0$  the intensities of the ground-state transitions are needed. Therefore, contributions of inelastic and cascade transitions have to be removed from the intensity distribution. We corrected the intensity distributions by simulating  $\gamma$ -ray cascades [32] from the levels in the whole energy range analogously to the strategy of the Monte Carlo code DICEBOX [33]. In these simulations, 1000 nuclear realizations starting from the ground state were created with level densities derived from experiments [34]. We applied the statistical methods also for the low-energy part of the level scheme instead of using experimentally known low-lying levels in  $^{89}\text{Y}$  because this would require knowledge of the partial decay widths of all transitions populating these fixed levels. Fluctuations of the nearest neighbor spacings were taken into account according to the Wigner distribution (see, e.g., Ref. [35]). The partial widths of the transitions to low-lying levels were assigned by using *a priori* known strength functions for  $E1$ ,  $M1$ , and  $E2$  transitions. Fluctuations of the partial widths were treated by applying the Porter-Thomas distribution [31].

In the present calculations, values of  $a = 9.39(16)$  MeV $^{-1}$  and  $E_1 = 0.32(6)$  MeV were used for the parameters of the back-shifted Fermi-gas (BSFG) model. These values were obtained from empirical formulas based on fits to experimental level densities [34]. In the individual nuclear realizations, the values of  $a$  and  $E_1$  were varied within their uncertainties. We assumed equal level densities for states with positive and negative parities at the same spin. This assumption has been recently justified by an investigation of level densities in the energy range from 5 to 10 MeV by using the  $^{90}\text{Zr}(^3\text{He}, ^3\text{H})$  reaction [36]. The level density calculated for levels with spin  $J = 3/2$  is compared with the density of the levels given in Table I in Fig. 9. The discrepancy between predicted level density and that of the resolved levels is consistent with the remarkable portion of strength in the continuum part of the intensity distribution. Note that the level density calculated in the BSFG model for the odd-mass nuclide  $^{89}\text{Y}$  is about 8 times greater than that for the even-even neighbors  $^{88}\text{Sr}$  [16]

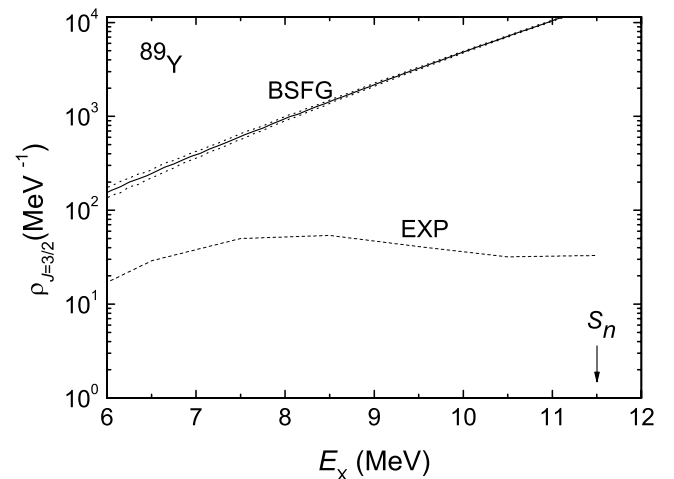


FIG. 9. Level densities of  $J = 3/2$  states as a function of excitation energy resulting from the BSFG model with the parameters taken from Ref. [34] and from the experimental levels listed in Table I (EXP).

and  $^{90}\text{Zr}$  [17]. Because the level density mainly influences the simulation of the  $\gamma$ -ray cascades, this fact causes many more possibilities for the de-excitation to low-lying levels and will on average result in smaller branching ratios for the ground-state transitions compared with those in the even-even neighbors.

For the  $E1$ ,  $M1$ , and  $E2$  photon strength functions, Lorentzian parametrizations [37] were used. The parameters of the Lorentzian for the  $E1$  strength were taken from a fit to  $(\gamma, n)$  data [38] in the energy range from 13 to 18 MeV, where the data were multiplied with a factor of 0.86 according to the findings of Ref. [39]. The resulting parameters are the position of the maximum  $E_0 = 16.76(1)$  MeV, the cross section at the maximum  $\sigma_0 = 191(1)$  mb, and the width  $\Gamma = 4.12(6)$  MeV. The maximum is slightly below the prediction of the Thomas-Reiche-Kuhn sum rule [40], which gives  $\sigma_0 = 203$  mb for the value of  $\Gamma$  given here. The parameters for the  $M1$  and  $E2$  strengths were taken from global parametrizations of  $M1$  spin-flip resonances and  $E2$  isoscalar resonances, respectively [41]. The influence of the shape of the  $E1$  strength function on the results of the simulations was tested by also applying a constant strength function and a Lorentzian with energy-dependent width in our recent study of  $^{98}\text{Mo}$  and  $^{100}\text{Mo}$  [30]. It turned out that only the Lorentzian with constant width, or, in the case of triaxial deformation, a combination of three Lorentzians, lead to consistency between input strength function and deduced photoabsorption cross section [30].

Spectra of  $\gamma$ -ray cascades were generated for groups of levels in 100-keV bins in each of the 1000 nuclear realizations. For illustration, intensity distributions of 10 individual nuclear realizations including transitions depopulating levels in 100-keV bins around 9 MeV are shown in Fig. 10. The spectra are characterized by a peak including the ground-state transitions from the levels in the considered energy bin and toward low energy by a broad distribution of inelastic transitions to low-lying levels. These spectra resemble qualitatively the ones measured in an experiment on  $^{90}\text{Zr}$  using tagged photons [42]. Because in the nuclear realizations the levels were created

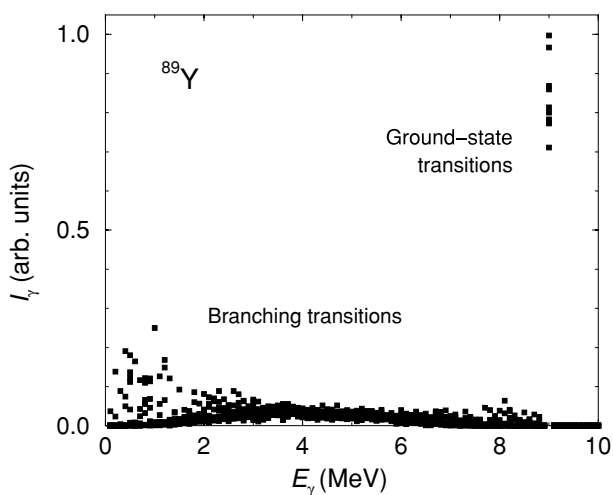


FIG. 10. Simulated intensity distribution of transitions depopulating levels in a 0.1-MeV bin around 9 MeV in  $^{89}\text{Y}$ . The squares depict the intensities obtained from 10 individual nuclear realizations.

randomly starting from the ground state instead of starting with the known first excited state at 0.9 MeV, the distribution of the branching transitions continues to the energy bin of the ground-state transitions.

Starting from the high-energy end of the experimental spectrum, which contains ground-state transitions only, the simulated intensities of the ground-state transitions were scaled to the experimental ones in the considered energy bin and the intensity distribution of the branching transitions was subtracted from the experimental spectrum. Applying this procedure step-by-step for each energy bin moving toward the low-energy end of the spectrum one obtains the intensity distribution of the ground-state transitions. Simultaneously, the branching ratios  $b_0^\Delta$  of the ground-state transitions are deduced for each energy bin  $\Delta$ . In an individual nuclear realization, the branching ratio  $b_0^\Delta$  is calculated as the ratio of the sum of the intensities of the ground-state transitions from all levels in  $\Delta$  to the total intensity of all transitions depopulating those levels to any low-lying levels including the ground state [16,17,30]. Through dividing the summed intensities in a bin of the experimental intensity distribution of the ground-state transitions by the corresponding branching ratio we obtain the absorption cross section for a bin as  $\sigma_\gamma^\Delta = \sigma_{\gamma\gamma}^\Delta / b_0^\Delta$ . Finally, the absorption cross sections of each bin were obtained by averaging over the values of the 1000 nuclear realizations. For the uncertainty of the absorption cross section a  $1\sigma$  deviation from the mean has been taken.

The branching ratios resulting from 10 individual realizations for all energy bins are shown in Fig. 11. They decrease in average from about 80% at 5 MeV, where the level density is small and only few inelastic transitions are possible, to about 40% at the neutron-separation energy. This percentage at about 11 MeV is considerably smaller than that of about 65% found for the even-even neighbors  $^{88}\text{Sr}$  [16] and  $^{90}\text{Zr}$  [17], which is a consequence of the higher level density in the odd-mass nuclide  $^{89}\text{Y}$  (see the earlier discussion). Note that an average

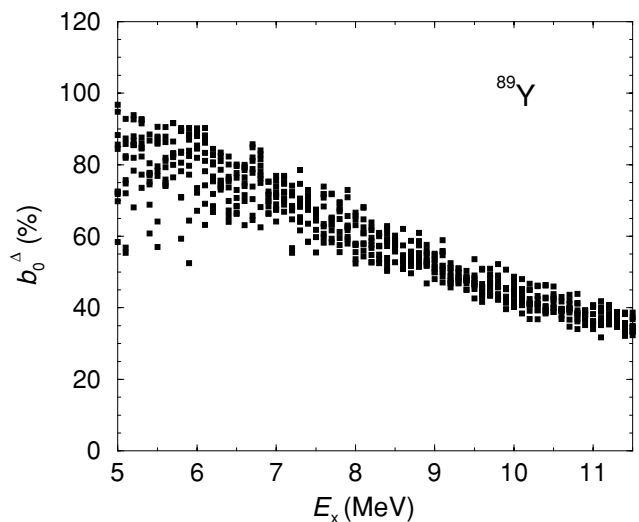


FIG. 11. Branching ratios of ground-state transitions obtained from the simulations of  $\gamma$ -ray cascades for  $^{89}\text{Y}$ . The squares represent the values of 10 individual nuclear realizations.

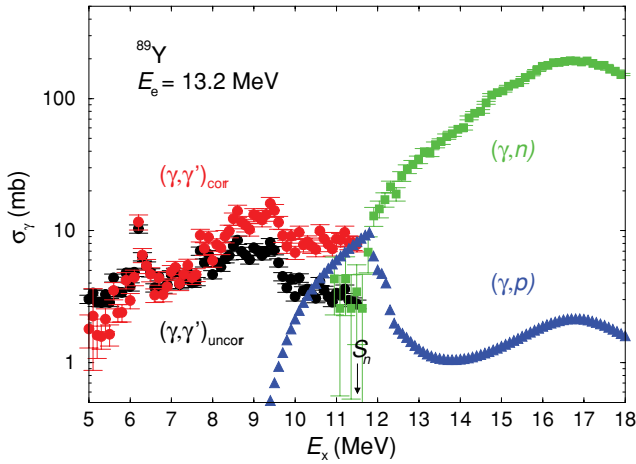


FIG. 12. (Color online) Uncorrected (black circles) and corrected (red circles) photoabsorption cross sections deduced from the measurement at  $E_e^{\text{kin}} = 13.2$  MeV in comparison with  $(\gamma, n)$  data [38] (green squares) and  $(\gamma, p)$  calculations [43] (blue triangles).

branching ratio is not representative for transitions with large intensities such as the resolved transitions given in Table I. It turned out from the simulations that the branching ratios of transitions with partial widths  $\Gamma_0$  such as the ones given in Table I are on the order of  $b_0 \approx 85\%$  to  $99\%$  [16]. Moreover, it was shown that the levels with the greatest integrated cross sections, amounting to a few percent of the number of levels predicted by the BSFG model, comprise most of the total integrated cross section of all levels, in quantitative agreement with the experimental findings [16].

The corrected photoabsorption cross sections are compared with the uncorrected values in Fig. 12. The effect of the subtraction of inelastic transitions at low energy and the enhancement resulting from division by the branching ratios at high energy are clearly visible. According to the correct treatment of the prominent levels, structural effects are not washed out by the statistical analysis but remain in the cross section (cf. Fig. 8). In addition to the cross sections deduced from the present  $(\gamma, \gamma')$  experiments, the  $(\gamma, n)$  data taken from Ref. [38] with the correction according to Ref. [39] and calculated  $(\gamma, p)$  cross sections [43] are shown in Fig. 12.

The total photoabsorption cross section has been deduced by combining the present  $(\gamma, \gamma')$  data with the  $(\gamma, n)$  data and with the calculated  $(\gamma, p)$  cross sections. This total cross section is compared with the Lorentz curve just described in Fig. 13. For comparison, the photoabsorption cross sections of the neighboring  $N = 50$  isotones  $^{88}\text{Sr}$  and  $^{90}\text{Zr}$  as taken from Refs. [16] and [17] are shown in Figs. 14 and 15, respectively. The experimental cross sections of the three isotones are very similar. All three include extra strength with respect to the approximation of the low-energy tail of the GDR by a Lorentz curve in the energy range from 6 to 11 MeV. In the case of  $^{90}\text{Zr}$ , this extra strength has been discussed as pygmy dipole strength [17]. In the following we will compare the dipole strength found in the three isotones with the results of calculations in the framework of a quasiparticle-random-phase approximation.

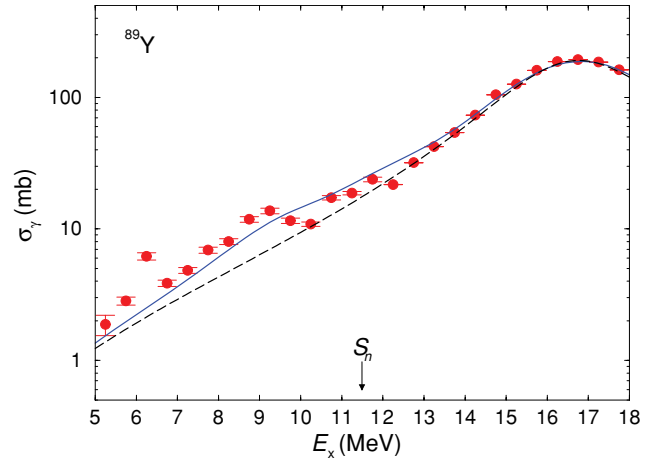


FIG. 13. (Color online) Total photoabsorption cross section of  $^{89}\text{Y}$  obtained by combining the present  $(\gamma, \gamma')$  data, the  $(\gamma, n)$  data of Ref. [38], and the  $(\gamma, p)$  calculations of Ref. [43]. The data were averaged over 0.5-MeV bins to reduce statistical fluctuations. The black dashed line represents a Lorentz distribution with the parameters given in the text. The blue solid line is the result of the QRPA calculations discussed in Sec. V.

## V. QUASIPARTICLE-RANDOM-PHASE APPROXIMATION CALCULATIONS

The quasiparticle-random-phase approximation (QRPA) is an appropriate model to describe the photoexcitation spectrum of both the vibrational states with individual levels below the neutron-separation energy and the hugely excited part of the continuous level structure at higher energies known as the GDR. The general outline of this standard model is presented in Refs. [40,44]. The present approach is described in detail in Ref. [45] and was also applied in our recent studies of the  $M1$  strength [46] and the  $E1$  strength [32,47] in the series of even-mass Mo isotopes with  $A = 92-100$ , which imply

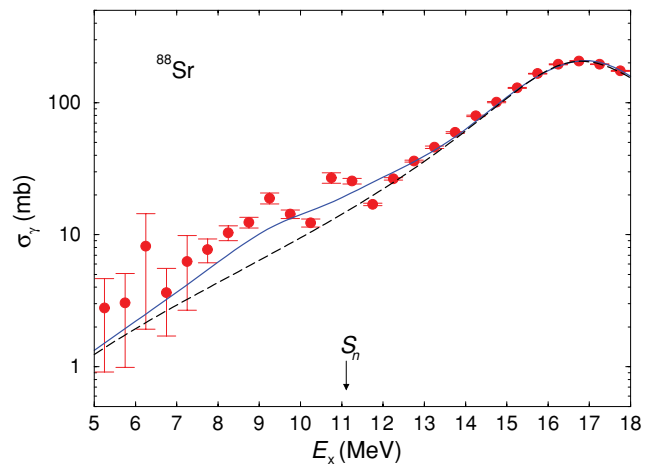


FIG. 14. (Color online) Total photoabsorption cross section of  $^{88}\text{Sr}$  as taken from Ref. [16]. The data were averaged over 0.5-MeV bins to reduce statistical fluctuations. The black dashed line represents a Lorentz distribution with the parameters given in Ref. [16]. The blue solid line is the result of the QRPA calculations discussed in Sec. V.

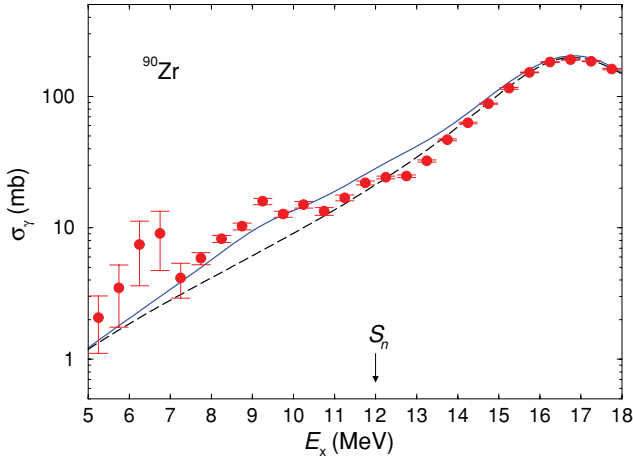


FIG. 15. (Color online) Total photoabsorption cross section of  $^{90}\text{Zr}$  as taken from Ref. [17]. The data were averaged over 0.5-MeV bins to reduce statistical fluctuations. The black dashed line represents a Lorentz distribution with the parameters given in Ref. [17]. The blue solid line is the result of the QRPA calculations discussed in Sec. V.

spherical as well as deformed nuclear shapes. The shapes of the nuclides  $^{88}\text{Sr}$ ,  $^{89}\text{Y}$ , and  $^{90}\text{Zr}$  considered here are assumed spherical because of the neutron-shell closure at  $N = 50$ . Our QRPA calculations are based on an empirical Hamiltonian with separable dipole-plus-octupole interactions given by the following expression:

$$H_{E1}^{\text{QRPA}} = h_{\text{MF}} - \frac{1}{2} \sum_{t=0,1} \sum_{\mu=-1,+1} \kappa_{1\mu}^t Q_{1\mu}^t Q_{1-\mu}^t - \frac{1}{2} \sum_{t=0,1} \sum_{\mu=-3,+3} \kappa_{3\mu}^t Q_{3\mu}^t Q_{3-\mu}^t. \quad (3)$$

The term  $h_{\text{MF}}$  is a quasiparticle Hamiltonian that consists of a Woods-Saxon mean field plus monopole pairing potential. The use of the Woods-Saxon potential is an improvement of the approach described in Ref. [45], which is based on a Nilsson potential. The interaction terms in the Hamiltonian, Eq. (3), comprise the isoscalar ( $t = 0$ ) and isovector ( $t = 1$ ) parts of the dipole-dipole ( $\lambda = 1$ ) and octupole-octupole interaction ( $\lambda = 3$ ), where the multipole operators are defined as  $Q_{\lambda\mu}^t = [r^\lambda Y_{\lambda\mu}]^\pi + (-1)^t [r^\lambda Y_{\lambda\mu}]^\nu$ . The constants  $\kappa_{\lambda\mu}^{t=1}$  of the repulsive isovector interaction are adjusted such that they reproduce the maximum of the GDR in accordance to the experimental value. To remove the effects of the spurious center-of-mass motion, which may contaminate the calculated  $E1$  strength, the suppression method described in Ref. [48] has been applied. This method allows us also to calculate the transition strengths without assuming any effective charge for the neutrons and using directly the bare proton charge  $e_\pi$  in the transition operator, that is,

$$\hat{M}(E1)_\mu = e_\pi \sum_{i=1}^Z [r Y_{1\mu}]_i. \quad (4)$$

The calculated  $E1$  photoabsorption cross sections for  $^{88}\text{Sr}$ ,  $^{89}\text{Y}$ , and  $^{90}\text{Zr}$  are shown in Figs. 14, 13, and 15, respectively. For

comparison with the experimental values the cross sections of the calculated QRPA states were folded with Lorentzians of 3.2 MeV width. This large width is needed to weep out the fluctuations of the cross sections that would appear when folding with a smaller width such as 500 keV as taken for averaging the experimental data. As a side effect of the long tails of the broad Lorentzians, part of the large  $E1$  strength is shifted from the GDR peak region toward the energy region below the neutron threshold, forming a smooth shape. Some structure effects of the QRPA states remain and appear as extra strength above the curve of the simple Lorentzian-like approximation of the GDR (cf. Figs. 14, 13, and 15). Interestingly, this extra strength is in qualitative agreement with the bump of the experimental cross sections in the energy range between about 6 and 11 MeV. Analogous calculations [17] for  $^{90}\text{Zr}$  have shown that the main part of this extra strength can be caused by an oscillation of the excessive neutrons against the  $N = Z$  neutron-proton core.

## VI. SUMMARY

We have studied the dipole-strength distribution in  $^{89}\text{Y}$  up to the neutron-separation energy in photon-scattering experiments at the ELBE accelerator using various electron energies. Ground-state transitions have been identified by comparing the transitions observed at different electron energies. We identified about 250 levels.

The intensity distribution obtained from the measured spectra after a correction for detector response and a subtraction of atomic background in the target contains a continuum part in addition to the resolved peaks. It turns out that below the neutron threshold the dipole strength in the resolved peaks amounts to about 20% of the total dipole strength whereas the continuum contains about 80%.

By means of simulations of  $\gamma$ -ray cascades, intensities of branching transitions to low-lying excited states could be estimated and subtracted from the experimental intensity distribution and the intensities of ground-state transitions could be corrected for their branching ratios.

A comparison of the photoabsorption cross section obtained in this way from the present ( $\gamma, \gamma'$ ) experiments with ( $\gamma, n$ ) data shows a smooth connection of the data of the two different experiments and gives new information about the extension of the dipole-strength function toward energies around and below the threshold of the ( $\gamma, n$ ) reaction. In comparison with an approximation of the GDR by a Lorentz curve we found extra  $E1$  strength in the energy range from 6 to 11 MeV, which is mainly concentrated in strong peaks.

QRPA calculations for the  $N = 50$  isotones  $^{88}\text{Sr}$ ,  $^{89}\text{Y}$ , and  $^{90}\text{Zr}$  also predict extra strength in the energy region from about 6 to 11 MeV, in qualitative agreement with the experimental findings.

## ACKNOWLEDGMENTS

We thank the staff of the ELBE accelerator for their cooperation during the experiments and acknowledge the technical assistance of A. Hartmann and W. Schulze. This work was supported by the Deutsche Forschungsgemeinschaft under Contract No. Do466/1-2.

- [1] A. Zilges, S. Volz, M. Babilon, T. Hartmann, P. Mohr, and K. Vogt, *Phys. Lett.* **B542**, 43 (2002).
- [2] S. Volz, N. Tsoneva, M. Babilon, M. Elvers, J. Hasper, R.-D. Herzberg, H. Lenske, K. Lindenberg, D. Savran, and A. Zilges, *Nucl. Phys.* **A779**, 1 (2006).
- [3] R. Mohan, M. Danos, and L. C. Biedenharn, *Phys. Rev. C* **3**, 1740 (1971).
- [4] Y. Suzuki, K. Ikeda, and H. Sato, *Prog. Theor. Phys.* **83**, 180 (1990).
- [5] J. Chambers, E. Zaremba, J. P. Adams, and B. Castel, *Phys. Rev. C* **50**, R2671 (1994).
- [6] F. Catara, E. G. Lanza, M. A. Nagarajan, and A. Vitturi, *Nucl. Phys.* **A624**, 449 (1997).
- [7] J. P. Adams, B. Castel, and H. Sagawa, *Phys. Rev. C* **53**, 1016 (1996).
- [8] P. G. Hansen, A. S. Jensen, and B. Jonson, *Annu. Rev. Nucl. Part. Sci.* **45**, 591 (1995).
- [9] E. Tryggestad, T. Aumann, T. Baumann, D. Bazin, J. R. Beene, Y. Blumenfeld, B. A. Brown, M. Chartier, M. L. Halbert, P. Heckman, J. F. Liang, D. C. Radford, D. Shapira, M. Thoennessen, and R. L. Varner, *Phys. Lett.* **B541**, 52 (2002).
- [10] K. Langanke and M. Wiescher, *Rep. Prog. Phys.* **64**, 1657 (2001).
- [11] T. Hartmann, J. Enders, P. Mohr, K. Vogt, S. Volz, and A. Zilges, *Phys. Rev. C* **65**, 034301 (2002).
- [12] T. Hartmann, M. Babilon, S. Kamedzhiev, E. Litvinova, D. Savran, S. Volz, and A. Zilges, *Phys. Rev. Lett.* **93**, 192501 (2004).
- [13] K. Govaert, F. Bauwens, J. Bryssinck, D. De Frenne, E. Jacobs, W. Mondelaers, L. Govor, and V. Yu. Ponomarev, *Phys. Rev. C* **57**, 2229 (1998).
- [14] N. Ryezayeva, T. Hartmann, Y. Kalmykov, H. Lenske, P. von Neumann-Cosel, V. Yu. Ponomarev, A. Richter, A. Shevchenko, S. Volz, and J. Wambach, *Phys. Rev. Lett.* **89**, 272502 (2002).
- [15] R. Schwengner, R. Beyer, F. Dönau, E. Grosse, A. Hartmann, A. R. Junghans, S. Mallion, G. Rusev, K. D. Schilling, W. Schulze, and A. Wagner, *Nucl. Instrum. Methods A* **555**, 211 (2005).
- [16] R. Schwengner, G. Rusev, N. Benouaret, R. Beyer, M. Erhard, E. Grosse, A. R. Junghans, J. Klug, K. Kosev, L. Kostov, C. Nair, N. Nankov, K. D. Schilling, and A. Wagner, *Phys. Rev. C* **76**, 034321 (2007).
- [17] R. Schwengner, G. Rusev, N. Tsoneva, N. Benouaret, R. Beyer, M. Erhard, E. Grosse, A. R. Junghans, J. Klug, K. Kosev, H. Lenske, C. Nair, K. D. Schilling, and A. Wagner, *Phys. Rev. C* **78**, 064314 (2008).
- [18] L. Funke, G. Winter, J. Döring, L. Käubler, H. Prade, R. Schwengner, E. Will, Ch. Protochristov, W. Andrejtscheff, L. G. Kostova, P. O. Lipas, and R. Wirowski, *Nucl. Phys.* **A541**, 241 (1992).
- [19] J. Reif, G. Winter, R. Schwengner, H. Prade, and L. Käubler, *Nucl. Phys.* **A587**, 449 (1995).
- [20] E. A. Stefanova, R. Schwengner, J. Reif, H. Schnare, F. Dönau, M. Wilhelm, A. Fitzler, S. Kasemann, P. von Brentano, and W. Andrejtscheff, *Phys. Rev. C* **62**, 054314 (2000).
- [21] M. Huber, P. von Neumann-Cosel, A. Richter, C. Schlegel, R. Schulz, J. J. Carroll, K. N. Taylor, D. G. Richmond, T. W. Sinor, C. B. Collins, and V. Yu. Ponomarev, *Nucl. Phys.* **A559**, 253 (1993).
- [22] P. Vogel and L. Kocbach, *Nucl. Phys.* **A176**, 33 (1971).
- [23] D. Kusnezov and F. Iachello, *Phys. Lett.* **B209**, 420 (1988).
- [24] A. Zilges, R.-D. Herzberg, P. von Brentano, F. Dönau, R. D. Heil, R. V. Jolos, U. Kneissl, J. Margraf, H. H. Pitz, and C. Wesselborg, *Phys. Rev. Lett.* **70**, 2880 (1993).
- [25] J. Reif, P. von Brentano, J. Eberth, J. Enders, R.-D. Herzberg, N. Huxel, L. Käubler, P. von Neumann-Cosel, N. Nicolay, N. Pietralla, H. Prade, A. Richter, C. Schlegel, H. Schnare, R. Schwengner, T. Servene, S. Skoda, H. G. Thomas, I. Wiedenhöver, G. Winter, and A. Zilges, *Nucl. Phys.* **A620**, 1 (1997).
- [26] CERN Program Library Long Writeup W5013, Geneva, 1993 (unpublished).
- [27] E. Haug, *Radiat. Phys. Chem.* **77**, 207 (2008).
- [28] G. Roche, C. Ducos, and J. Proriot, *Phys. Rev. A* **5**, 2403 (1972).
- [29] F. Salvat, J. D. Martinez, R. Mayol, and J. Parellada, *Phys. Rev. A* **36**, 467 (1987).
- [30] G. Rusev, R. Schwengner, F. Dönau, M. Erhard, E. Grosse, A. R. Junghans, K. Kosev, K. D. Schilling, A. Wagner, F. Bečvář, and M. Krtička, *Phys. Rev. C* **77**, 064321 (2008).
- [31] C. E. Porter and R. G. Thomas, *Phys. Rev.* **104**, 483 (1956).
- [32] G. Rusev, dissertation, Technische Universität Dresden, 2007, Report FZD-478, <http://fzd.de/publications/010008/10008.pdf>.
- [33] F. Bečvář, *Nucl. Instrum. Methods A* **417**, 434 (1998).
- [34] T. von Egidy and D. Bucurescu, *Phys. Rev. C* **72**, 044311 (2005).
- [35] T. A. Brody, J. Flores, J. B. French, P. A. Mello, A. Pandey, and S. S. M. Wong, *Rev. Mod. Phys.* **53**, 385 (1981).
- [36] Y. Kalmykov, T. Adachi, G. P. A. Berg, H. Fujita, K. Fujita, Y. Fujita, K. Hatanaka, J. Kamiya, K. Nakanishi, P. von Neumann-Cosel, V. Yu. Ponomarev, A. Richter, N. Sakamoto, Y. Sakemi, A. Shevchenko, Y. Shimbara, Y. Shimizu, F. D. Smit, T. Wakasa, J. Wambach, and M. Yosoi, *Phys. Rev. Lett.* **96**, 012502 (2006).
- [37] P. Axel, *Phys. Rev.* **126**, 671 (1962).
- [38] A. Lepretre, H. Beil, R. Bergere, P. Carlos, A. Veyssiere, and M. Sugawara, *Nucl. Phys.* **A175**, 609 (1971); <http://www-nds.iaea.org/exfor/>.
- [39] B. L. Berman, R. E. Pywell, S. S. Dietrich, M. N. Thompson, K. G. McNeill, and J. W. Jury, *Phys. Rev. C* **36**, 1286 (1987).
- [40] P. Ring and P. Schuck, *The Nuclear Many Body Problem* (Springer-Verlag, Berlin, Heidelberg, 1980).
- [41] T. Belgia, O. Bersillon, R. Capote, T. Fukahori, G. Zhitang, S. Goriely, M. Herman, A. V. Ignatyuk, S. Kailas, A. Koning, P. Oblozinsky, V. Plujko, and P. Young, *Handbook for Calculations of Nuclear Reaction Data, RIPL-2*, IAEA-TECDOC-1506 (IAEA, Vienna, 2006); <http://www-nds.iaea.org/RIPL-2/>.
- [42] R. Alarcon, R. M. Laszewski, A. M. Nathan, and S. D. Hoblit, *Phys. Rev. C* **36**, 954 (1987).
- [43] A. J. Koning, S. Hilaire, and M. C. Duijvestijn, *AIP Conf. Proc.* **769**, 1154 (2005).
- [44] D. J. Rowe, *Nuclear Collective Motion* (Methuen, London, 1970).
- [45] F. Dönau, G. Rusev, R. Schwengner, A. R. Junghans, K. D. Schilling, and A. Wagner, *Phys. Rev. C* **76**, 014317 (2007).
- [46] G. Rusev, R. Schwengner, F. Dönau, M. Erhard, S. Frauendorf, E. Grosse, A. R. Junghans, L. Käubler, K. Kosev, L. K. Kostov,

S. Mallion, K. D. Schilling, A. Wagner, H. von Garrel, U. Kneissl, C. Kohstall, M. Kreuz, H. H. Pitz, M. Scheck, F. Stedile, P. von Brentano, C. Fransen, J. Jolie, A. Linnemann, N. Pietralla, and V. Werner, *Phys. Rev. C* **73**, 044308 (2006).

[47] R. Schwengner, N. Benouaret, R. Beyer, F. Dönau, M. Erhard, S. Frauendorf, E. Grosse, A. R. Junghans, J. Klug, K. Kosev, C. Nair, N. Nankov, G. Rusev, K. D. Schilling, and A. Wagner, *Nucl. Phys.* **A788**, 331c (2007).

[48] F. Dönau, *Phys. Rev. Lett.* **94**, 092503 (2005).